

THE PROPERTIES OF THE PROGENITOR SUPERNOVA, PULSAR WIND, AND NEUTRON STAR INSIDE  
PWN G54.1+0.3

JOSEPH D. GELFAND

NYU Abu Dhabi and  
P.O. Box 903, New York, NY 10276, USA  
Harvard-Smithsonian Center for Astrophysics and  
60 Garden Street, Cambridge, MA 02138, USA

TEA TEMIM

Observational Cosmology Lab, Code 665  
NASA Goddard Space Flight Center and  
Greenbelt, MD 20771, USA*Draft version April 5, 2024*

## ABSTRACT

The evolution of a pulsar wind nebula (PWN) inside a supernova remnant (SNR) is sensitive to properties of the central neutron star, pulsar wind, progenitor supernova, and interstellar medium. These properties are both difficult to measure directly and critical for understanding the formation of neutron stars and their interaction with the surrounding medium. In this paper, we determine these properties for PWN G54.1+0.3 by fitting its observed properties with a model for the dynamical and radiative evolution of a PWN inside an SNR. Our modeling suggests that the progenitor of G54.1+0.3 was an isolated  $\sim 15 - 20 M_{\odot}$  star which exploded inside a massive star cluster, creating a neutron star initially spinning with period  $P_0 \sim 30 - 80$  ms. We also find that  $\gtrsim 99.9\%$  of the pulsar’s rotational energy is injected into the PWN as relativistic electrons and positrons whose energy spectrum is well characterized by a broken power-law. Lastly, we propose future observations which can both test the validity of this model and better determine the properties of this source – in particular, its distance and the initial spin period of the central pulsar.

*Subject headings:* pulsars: individual: PSR J1930+1852, ISM: individual objects: PWN G54.1+0.3, ISM: supernova remnants, X-rays: individual: PWN G54.1+0.3

## 1. INTRODUCTION

Stars born with a mass  $\gtrsim 8 M_{\odot}$  (e.g., Heger et al. 2003) are believed to end their lives in a core-collapse supernova powered by the gravitational collapse of its iron core into a neutron star (e.g. Zwicky 1938). In many cases, this collapse creates a rapidly spinning (initial rotational period  $P_0 \ll 1$  s) neutron star with a strong ( $B \sim 10^{12}$  G) surface magnetic field observed as a pulsar. The rotational energy of such neutron stars powers a magnetized, highly relativistic outflow called a pulsar wind (Goldreich & Julian 1969; Arons 2002). The confinements of this outflow creates a “termination shock” (Kennel & Coroniti 1984b; see Gaensler & Slane 2006 for a recent review), and the post-shock (“downstream”) pulsar wind creates a pulsar wind nebula (PWN) as it expands into its surroundings. When the neutron star is very young, it is located inside the supernova remnant (SNR) created by the expansion of the material

the properties of the progenitor supernova (e.g., the mass and initial kinetic energy of the supernova ejecta; Kennel & Coroniti 1984a, Gelfand et al. 2009 and references therein) – quantities difficult to measure directly but vital for understanding the physics of core-collapse supernovae.

Currently, the best way of measuring the properties of the central neutron star, its pulsar wind, and progenitor supernova requires modeling the dynamical and radiative evolution of a PWN inside an SNR (e.g. Reynolds & Chevalier 1984; Gelfand et al. 2009; Tanaka & Takahara 2010; Bucciantini et al. 2011, again see Gaensler & Slane 2006 for a recent review). Such models have been developed, incorporating the effect of the spin-down of the central neutron star (e.g. Bucciantini et al. 2004; Gelfand et al. 2007, 2009), the evolution of the surrounding SNR as it expands into the ISM (e.g. Gelfand et al. 2007, 2009), and for different properties of the pulsar winds after being injected into

possible parameter space and identify degeneracies between parameters, and in Section 3.2.1 compare our derived properties of the neutron star, pulsar wind, progenitor supernova, and surrounding ISM with the results of previous analyses to determine the impact of our assumptions. In Section 4, we discuss the implications of these results concerning the progenitor of this system (Section 4.1), the formation of its associated pulsar (Section 4.2), and both the production and acceleration of particles in the pulsar wind (Section 4.3). Finally, in Section 5, we use our model to predict the results of future observations of this source and discuss their potential implications. Lastly, in Section 6, we summarize our results.

## 2. EVOLUTIONARY MODEL

Our model for dynamical and radiative evolution of a PWN inside an SNR is closely based on that developed by Gelfand et al. (2009). We assume the rotational luminosity  $\dot{E}$  of the central neutron star evolves as (e.g. Gaensler & Slane 2006)

$$\dot{E}(t) = \dot{E}_0 \left( 1 + \frac{t}{\tau_{\text{sd}}} \right)^{-\frac{p+1}{p-1}}, \quad (1)$$

where  $t$  is the time since the progenitor supernova,  $\dot{E}_0$  is the neutron star’s initial spin-down luminosity,  $\tau_{\text{sd}}$  is neutron star’s “spin-down” timescale, and  $p$  is the neutron star’s braking index (Gelfand et al. 2009), and that all of the rotational energy of the neutron star is carried away by the pulsar wind generated in its magnetosphere. We further assume that, immediately after the pulsar wind is injected into the PWN at the termination shock, a constant fraction  $\eta_B$  of its energy is in the form of magnetic fields, while the rest  $1 - \eta_B$  is in the kinetic energy of electrons and positrons (Gelfand et al. 2009). Theoretical studies predict that, under most physical conditions, the spectrum of these particles is well described by a relativistic Maxwellian with a high-energy power-law tail (e.g., Spitkovsky 2008; Sironi & Spitkovsky 2011). While this spectrum can reproduce the broadband spectral energy distribution (SED) of some PWNe (e.g., Fang & Zhang 2010), we find it does not work for G54.1+0.3 for constant parameters. Instead, we use a broken power-law inject spectrum, which recent simulations (e.g., Sironi & Spitkovsky 2011; Sironi et al. 2013) are able to produce under certain physical condition, and has been used to reproduce the broadband SED of this PWN and others in similar work (e.g. Chevalier 2005; Bucciantini et al. 2011; Torres et al. 2014). In this case, the injected particle spectrum is:

calculate  $n_{\text{break}}(t)$  by requiring that:

$$(1 - \eta_B) \dot{E} = \int_{E_{\text{min}}}^{E_{\text{max}}} E n(E) dE \quad (3)$$

at all times.

To minimize the number of free parameters, we assume that all parameters related to the properties of the pulsar wind ( $\eta_B$ ,  $E_{\text{min}}$ ,  $E_{\text{break}}$ ,  $E_{\text{max}}$ ,  $p_1$ ,  $p_2$ ) remain constant with time – in contrast to other models which assume different temporal evolution’s for (some) of these parameters. For example, Bucciantini et al. (2011) assume that  $E_{\text{max}}$  is proportional to the electric potential of the pulsar’s magnetosphere  $\Phi$ , while others set  $E_{\text{max}}$  to the particle energy whose Larmor radius is the equal to the the radius of the termination shock (e.g., Torres et al. 2014) or the PWN itself (e.g., Li et al. 2010). In Section 3.2.1, we estimate the systematic uncertainty resulting from these different assumptions by comparing our result to those derived from different models. We also note that our model does not consider the possibility of ions in the pulsar wind, nor the magnetic reconnection and particle acceleration beyond (“downstream”) of the termination shock as predicted by recent 3D simulations of these systems (e.g., Porth et al. 2013, 2014). These processes are expected to primarily affect the spectral evolution of the PWN (e.g., Olmi et al. 2014), and are left for future work.

As done by Gelfand et al. (2009), the dynamical evolution of the PWN is determined by the motion of the surrounding shell of swept-up material. This shell is subject to a net force resulting for the difference in pressure between the PWN and the SNR just outside the PWN. We calculate the pressure just outside the PWN using the procedure described by Gelfand et al. (2009), which assumes the initial density profile of the supernova ejecta is a uniform density inner core surrounded by an envelope whose density decreases as  $\rho \propto r^{-9}$ , where  $r$  is the distance from the center of the SNR, and that the SNR is expanding into a constant density ISM.

As done by Gelfand et al. (2009), we calculate the pressure inside the PWN assuming that both the PWN’s magnetic field strength  $B_{\text{pwn}}$  and the particle density are spatially uniform – i.e., using a “one-zone” model for the PWN. We account for both adiabatic and radiative losses (assumed to be dominated by synchrotron emission and inverse Compton scattering off Cosmic Microwave Background photons) of the electrons and positrons inside the PWN. The spectrum of photons generated by the radiative losses are calculated using the same procedure described in Gelfand et al. (2009). To minimize the number of free parameters in our model, we do not consider emis-

In Section 3.1, we present the observed properties of G54.1+0.3, and in Section 3.2 describe the algorithm used to determining which combinations of model parameters are able to reproduce them. Finally, we compare our results with similar work (Section 3.2.1).

### 3.1. Observed Properties

G54.1+0.3 is one of the best studied PWNe in the Milky Way. Associated with radio (Camilo et al. 2002) and X-ray (Lu et al. 2007) pulsar PSR J1930+1852, it is also detected across the electromagnetic spectrum. This PWN has a similar extent at both radio and X-ray energies (Lu et al. 2001; Lang et al. 2010), with a semi-major axis of  $\sim 1'.25$  and a semi-minor axis of  $\sim 1'.0$  (Lang et al. 2010). Since our model assumes a spherically symmetric PWN (Section 2), we set the angular size of the PWN  $\theta_{\text{pwn}}$  our model must reproduce to the “average” of its measured semi-minor and semi-major axes, and use these to determine the  $3\sigma$  lower and upper limits on  $\theta_{\text{pwn}}$  (Table 1). We also require our model to reproduce its volume-integrated radio (Lang et al. 2010), X-ray (Temim et al. 2010), and TeV  $\gamma$ -ray (Acciari et al. 2010) properties, listed in Table 1. We do not attempt to reproduce the mid-infrared (mid-IR) properties of G54.1+0.3 (Koo et al. 2008; Temim et al. 2010) since this emission is dominated by material shocked and heated by the expanding PWN. Because we are using a one-zone model (Section 2), we also do not attempt to any reproduce spatial variations in its emission (e.g., Lu et al. 2001; Temim et al. 2010).

Lastly, we require our model to reproduce the size of the SNR. The SNR around PWN G54.1+0.3 has been detected at both radio (Lang et al. 2010) and X-ray (Bocchino et al. 2010) energies, each reporting a somewhat different angular radius  $\theta_{\text{snr}}$ . To resolve this discrepancy, we analyzed an archival D-array 1.4 GHz VLA observation of this PWN, estimating an SNR angular radius of  $\approx 6'.6$ . We then estimated the error on  $\theta_{\text{snr}}$  by setting  $3\sigma$  upper and lower limits to those reported by Lang et al. (2010) and Bocchino et al. (2010).

As listed in Table 1, our model has to reproduce twelve different observed quantities – equal to the number of model parameters. As a result, our fit has zero degrees of freedom. While the distance  $d$  to G54.1+0.3 is a free parameter in our model (Table 1), the fitting algorithm described in Section 3.2 favors  $d = 4.5 - 9$  kpc, as derived from an analysis of its HI absorption spectrum (Leahy et al. 2008).

### 3.2. Model Fit

To derive the physical properties of the central neu-

2002), we set the true age  $t_{\text{age}}$  of G54.1+0.3 to:

$$t_{\text{age}} = \frac{2\tau_{\text{ch}}}{p-1} - \tau_{\text{sd}}, \quad (4)$$

and the initial spin-down luminosity  $\dot{E}_0$  of this pulsar to:

$$\dot{E}_0 = \dot{E} \left( 1 + \frac{t_{\text{age}}}{\tau_{\text{sd}}} \right)^{\frac{p+1}{p-1}}, \quad (5)$$

where  $p$  and  $\tau_{\text{sd}}$  are respectively the pulsar’s braking index and spin-down timescale.

For a given combination, we first determine the model-predicted value of each observable  $\mathcal{M}$ . We then calculate the likelihood  $\mathcal{L}(\mathcal{D}|\theta)$  this set of parameters accurately represents the data:

$$\mathcal{L}(\mathcal{D}|\theta) = \prod_{i=1}^{12} \frac{1}{\sqrt{2\pi}\sigma_i} e^{-\frac{1}{2}\left(\frac{\mathcal{M}_i - \mathcal{D}_i}{\sigma_i}\right)^2}, \quad (6)$$

where  $\sigma_i$  is the error on each observed quantity. The MCMC algorithm then searches the possible 12-dimensional parameter space for the combinations with the largest  $\ln \mathcal{L}$ :

$$\ln \mathcal{L} = \sum_{i=1}^{12} \left[ \ln \left( \frac{1}{\sqrt{2\pi}\sigma_i} \right) - \frac{1}{2} \left( \frac{\mathcal{M}_i - \mathcal{D}_i}{\sigma_i} \right)^2 \right] \quad (7)$$

$$= -\frac{1}{2}\chi^2 + C, \quad (8)$$

where  $\chi^2$  is defined as:

$$\chi^2 = \sum_{i=1}^{12} \left( \frac{\mathcal{M}_i - \mathcal{D}_i}{\sigma_i} \right)^2, \quad (9)$$

and  $C$  is the same for all combinations. Therefore, maximizing  $\ln \mathcal{L}$  is equivalent to minimizing  $\chi^2$ . It conducts this search using the following procedure:

1. For a given combination  $\theta_n$ , evaluate  $\ln \mathcal{L}_n$ .
2. Propose  $\theta_{n+1}$  which is  $\theta_n + f(\theta)$ , where  $f(\theta)$  is a set of random, zero-mean, Gaussian distributed numbers whose width varies for each model parameter.
3. Calculate  $\ln \mathcal{L}_{n+1}$  for the proposed  $\theta_{n+1}$ .
4. If  $\frac{\mathcal{L}_{n+1}}{\mathcal{L}_n} \geq \delta$ , where  $\delta$  is a random, Gaussian distributed number between 0 and 1, then  $\theta_{n+2}$  is calculated with  $\theta_{n+1}$  as a starting point. Otherwise,  $\theta_{n+2}$  is calculated with  $\theta_n$  as a starting point.

The width of  $f(\theta)$  was chosen such that the  $\theta_{n+1}$  satisfies

**Table 1**  
The Set of Model Parameters with the Lowest  $\chi^2$  ( $\chi^2 \approx 4.10$ ), Their Predicted Properties of G54.1+0.3, and the Observed Values of These Quantities.

Model Input Parameters		Predicted Observables		
Parameter	VALUE	Observable	OBSERVED VALUE	PREDICTED VALUE
$\log(E_{\text{sn}}/10^{51} \text{ ergs})$	-0.03	$\theta_{\text{snr}}$	$6.6 \pm 0.4$	6.5
$\log(M_{\text{ej}}/M_{\odot})$	1.34	$\theta_{\text{pwn}}$	$1.14 \pm 0.04$	1.12
$\log(n_{\text{ism}}/\text{cm}^{-3})$	-2.29	1.4 GHz Flux Density	$433 \pm 30 \text{ Jy}$	429 Jy
Distance (kpc)	4.90	4.7 GHz Flux Density	$327 \pm 25 \text{ Jy}$	329 Jy
$p$	2.94	8.5 GHz Flux Density	$252 \pm 20 \text{ Jy}$	257 Jy
$\log(\tau_{\text{sd}}/1 \text{ year})$	2.90	$F_{\text{X},2-10}$	$(5.43 \pm 0.035) \times 10^{-12} \frac{\text{ergs}}{\text{s cm}^2}$	$5.43 \times 10^{-12} \frac{\text{ergs}}{\text{s cm}^2}$
$\log(\eta_{\text{B}})$	-3.14	$\Gamma$	$2.09 \pm 0.01$	$2.09 \pm 0.002$
$\log(E_{\text{min}}/\text{GeV})$	1.05	311 GeV Photon Density	$(1.10 \pm 0.56) \times 10^{-11} \frac{\text{photons}}{\text{cm}^2 \text{ s TeV}}$	$0.80 \times 10^{-11} \frac{\text{photons}}{\text{cm}^2 \text{ s TeV}}$
$\log(E_{\text{break}}/\text{GeV})$	3.45	492 GeV Photon Density	$(4.2 \pm 1.4) \times 10^{-12} \frac{\text{photons}}{\text{cm}^2 \text{ s TeV}}$	$3.1 \times 10^{-12} \frac{\text{photons}}{\text{cm}^2 \text{ s TeV}}$
$\log(E_{\text{min}}/\text{GeV})$	6.98	780 GeV Photon Density	$(1.12 \pm 0.45) \times 10^{-12} \frac{\text{photons}}{\text{cm}^2 \text{ s TeV}}$	$1.21 \times 10^{-12} \frac{\text{photons}}{\text{cm}^2 \text{ s TeV}}$
$p_1$	1.84	1.2 TeV Photon Density	$(6.2 \pm 1.7) \times 10^{-13} \frac{\text{photons}}{\text{cm}^2 \text{ s TeV}}$	$4.9 \times 10^{-13} \frac{\text{photons}}{\text{cm}^2 \text{ s TeV}}$
$p_2$	2.77	3 TeV Photon Density	$(3.9 \pm 2.1) \times 10^{-14} \frac{\text{photons}}{\text{cm}^2 \text{ s TeV}}$	$7.2 \times 10^{-14} \frac{\text{photons}}{\text{cm}^2 \text{ s TeV}}$

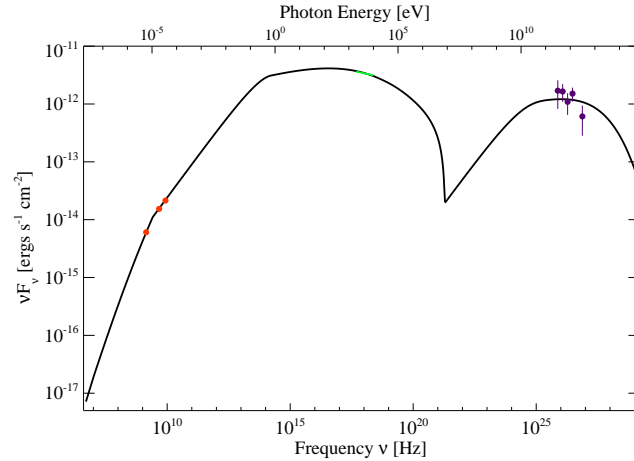


**Figure 1.** The broadband spectral energy diagram of PWN G54.1+0.3 predicted by the model described in Section 2 for the parameters listed in Table 1. The red, green, and purple points are, respectively, the observed radio, X-ray, and TeV  $\gamma$ -ray emission (Section 3.1, Table 1).

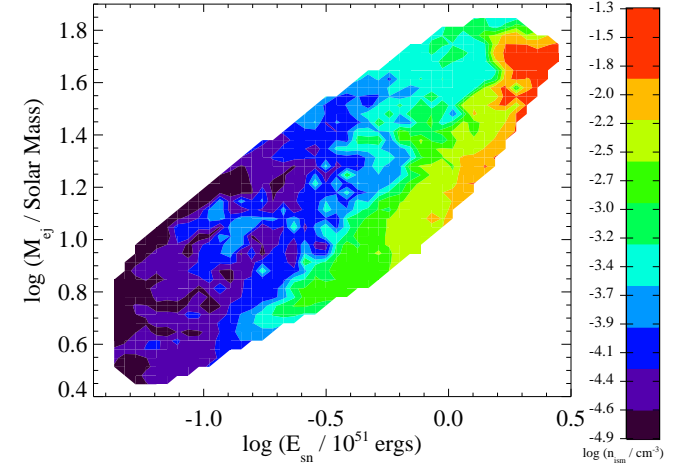


**Figure 2.** The ISM density  $n_{\text{ism}}$  (color scale) for different values of the initial kinetic energy  $E_{\text{sn}}$  and mass  $M_{\text{ej}}$  of the supernova ejecta for trials with  $\chi^2 < 7.10$  (the  $3\sigma$  parameter space).

tion coefficient  $r_{xy}$ , defined to be:

$$r_{xy} = \frac{\sum_{i=1}^N (x_i - \bar{x})(y_i - \bar{y})}{\sqrt{\sum_{i=1}^N (x_i - \bar{x})^2} \sqrt{\sum_{i=1}^N (y_i - \bar{y})^2}}, \quad (10)$$

in Figure 1, this set of parameters accurately reproduces the broadband SED of this PWN.

Our search of parameter space allows us to estimate the (statistical) confidence interval of a given parameter by first ordering, from lowest to highest, its value

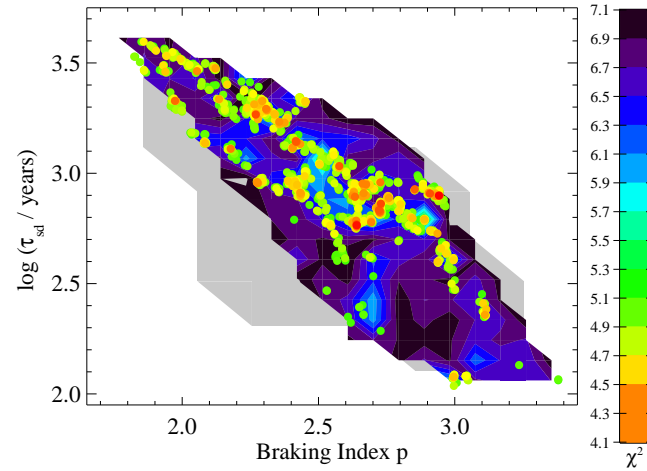
between each pair of model parameters  $x$  and  $y$ , where  $\bar{x}$  and  $\bar{y}$  are their average values,  $x_i$  and  $y_i$  are their values for a particular trial, and  $N$  is the number of trials, using only trials with  $\chi^2 < 7.10$  (spanning the  $3\sigma$  parameter

**Table 2**

Linear Pearson Correlation coefficient  $r_{xy}$  (Equation (10)) between the model parameters as calculated for all trials with  $\chi^2 < 7.10$ .

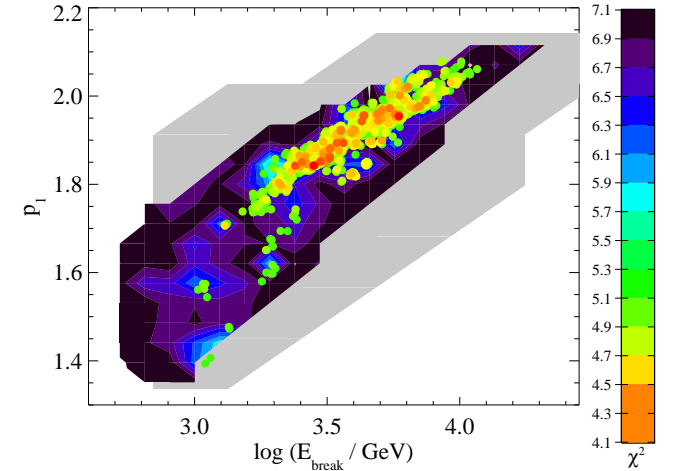
	$\log E_{\text{sn}}$	$\log M_{\text{ej}}$	$\log n_{\text{ism}}$	$p$	$\log \tau_{\text{sd}}$	$\log \eta_{\text{B}}$	$\log E_{\text{max}}$	$\log E_{\text{min}}$	$p_1$	$\log E_{\text{break}}$	$p_2$	$d$
$\log E_{\text{sn}}$	<b>1.00</b>	<b>0.87</b>	<b>0.82</b>	-0.12	0.03	0.22	-0.35	0.13	0.16	0.18	-0.17	0.23
$\log M_{\text{ej}}$	<b>0.87</b>	<b>1.00</b>	<b>0.59</b>	-0.18	-0.12	-0.07	-0.29	-0.19	-0.23	-0.15	-0.49	0.37
$\log n_{\text{ism}}$	<b>0.82</b>	<b>0.59</b>	<b>1.00</b>	-0.31	0.44	-0.01	-0.43	0.13	0.18	0.04	0.25	-0.33
$p$	-0.12	-0.18	-0.31	<b>1.00</b>	<b>-0.83</b>	-0.04	0.01	0.01	-0.13	-0.01	-0.01	0.09
$\log \tau_{\text{sd}}$	0.03	-0.12	0.44	<b>-0.83</b>	<b>1.00</b>	0.05	-0.11	0.18	0.36	0.12	0.42	-0.48
$\log \eta_{\text{B}}$	0.22	-0.07	-0.01	-0.04	0.05	<b>1.00</b>	0.09	0.49	<b>0.68</b>	<b>0.73</b>	-0.05	<b>0.54</b>
$\log E_{\text{max}}$	-0.35	-0.29	-0.43	0.01	-0.11	0.09	<b>1.00</b>	0.14	0.04	0.15	0.13	0.17
$\log E_{\text{min}}$	0.13	-0.19	0.13	0.01	0.18	0.49	0.14	<b>1.00</b>	<b>0.78</b>	<b>0.68</b>	0.35	0.07
$p_1$	0.16	-0.23	0.18	-0.13	0.36	<b>0.68</b>	0.04	<b>0.78</b>	<b>1.00</b>	<b>0.93</b>	0.40	0.12
$\log E_{\text{break}}$	0.18	-0.15	0.04	-0.01	0.12	<b>0.73</b>	0.15	<b>0.68</b>	<b>0.93</b>	<b>1.00</b>	0.28	0.36
$p_2$	-0.17	-0.49	0.25	-0.01	0.42	-0.05	0.13	0.35	0.40	0.28	<b>1.00</b>	<b>-0.71</b>
$d$	0.23	0.37	-0.33	0.09	-0.48	<b>0.54</b>	0.17	0.07	0.12	0.36	<b>-0.71</b>	<b>1.00</b>

Note: Values in bold indicates that  $|r_{xy}| \geq 0.5$ , indicating a significant degeneracy between the two parameters.

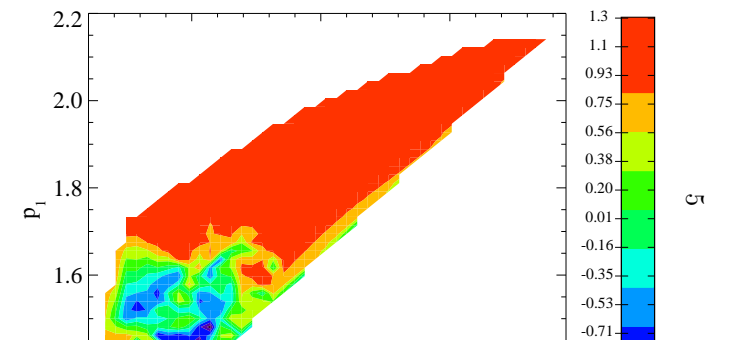


**Figure 3.** The  $\chi^2$  for trials with different values of the braking index  $p$  and spin-down timescale  $\tau_{\text{sd}}$  of PSR J1930+1852, with red signifying a lower  $\chi^2$  (better fit) and black a higher  $\chi^2$  (worse fit). The dots indicate trials with  $\chi^2 < 5.10$  and are included to better demonstrate the degeneracy between these two parameters. The clumpiness of these points primarily reflects the sampling of the parameter space by our MCMC algorithm.

degenerate, with a more energetic supernova explosion requiring a larger ejecta mass occurring in a denser environment (Figure 2). A similar degeneracy was reported in a recent analysis of Kes 75, which discusses possible physical origins for this behavior (Gelfand et al. 2014). The pulsar braking index  $p$  and spin-down timescale  $\tau_{\text{sd}}$  are also strongly degenerate, with higher values of  $p$  requiring lower values of  $\tau_{\text{sd}}$  (Figure 3). The break energy  $E_{\text{break}}$  in the spectrum of particles injected at the termination shock strongly depends on the low energy particle index  $p_1$ , with higher values of  $E_{\text{break}}$  requiring a “softer” (higher values of  $p_1$ ) particle spectrum (Figure



**Figure 4.** The  $\chi^2$  for trials with different values of the break energy  $E_{\text{break}}$  and low-energy particle index  $p_1$ , with red signifying a lower  $\chi^2$  (better fit) and black a higher  $\chi^2$  (worse fit). The dots indicate trials with  $\chi^2 < 5.10$  and are included to better demonstrate the degeneracy between these two parameters. The clumpiness of these points primarily reflects the sampling of the parameter space by our MCMC algorithm.



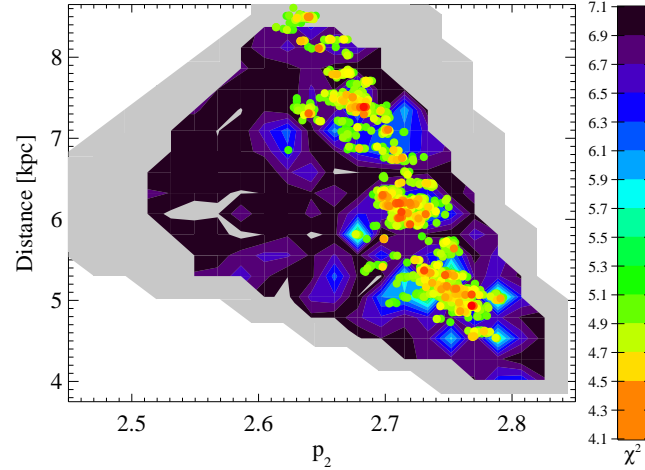


**Figure 6.** The  $\chi^2$  for trials with different values of the high-energy particle index  $p_2$  and distance  $d$  to G54.1+0.3, with red signifying a lower  $\chi^2$  (better fit) and black a higher  $\chi^2$  (worse fit). The dots indicate trials with  $\chi^2 < 5.10$  and are included to better demonstrate the degeneracy between these two parameters. The clumpiness of these points primarily reflects the sampling of the parameter space by our MCMC algorithm.

energy  $E_{\text{break}}$  (and correspondingly higher values of  $p_1$ ) and a larger distance  $d$  (and correspondingly lower values of  $p_2$ ).

### 3.2.1. Comparison with Other models

In this section, we compare our results with those obtained using other models for the evolution of a PWN inside a SNR to determine how our analysis is affected by the assumptions made by our model described in Section 2 – allowing us to estimate the systematic uncertainty of this approach. The results of these different models are provided in Table 3.

Chevalier (2005) uses the measured spectral properties and radius of this PWN and the spin-down properties of the central pulsar to primarily estimate the birth properties of the neutron star, assuming  $M_{\text{ej}} \equiv 5 M_{\odot}$  and  $E_{\text{sn}} = 10^{51}$  ergs – a combination not favored by our fits (Figure 2). He did not attempt to reproduce the broadband SED, and set  $p_1$  and  $p_2$  to values inferred from single power-law fits to the observed radio and X-ray spectrum. While the value of  $p_2$  derived from this method agrees with our value, the value of  $p_1$  does not since, for  $E_{\text{min}} \approx 10$  GeV, the SED predicted by our model contains a spectral break between 1.4 and 4.8 GHz (Figure 1). Additionally, he assumes that  $\eta_B = \frac{3}{7}$  (Chevalier 2005), significantly higher value than allowed by our fits. The higher value of  $\eta_B$  decreases the particle energy inside the PWN, resulting in an initial period  $P_0$

$(0.5 - 1.6) \times 10^{51}$  ergs and  $t_{\text{age}} \sim 1800 - 2400$  years if the ions are  $\sim 2\times$  hotter than the electrons. Both sets of  $E_{\text{sn}}$  and  $t_{\text{age}}$  are consistent with our results (Table 3). They also found that  $M_{\text{ej}} = 8 M_{\odot}$ ,  $p = 3$ , and  $\tau_{\text{sd}} = 500$  years can reproduce the radius of the PWN and SNR (Bocchino et al. 2010) – in agreement with our results. Since they did not attempt to reproduce the broadband SED of this source, this analysis does not constrain the magnetization or spectrum of particles injected into the PWN at the termination shock.

G54.1+0.3 was also analyzed by Tanaka & Takahara (2011), who reproduce both the size and broadband SED of this PWN using a model very similar to ours (Section 2) but include inverse Compton scattering of electrons off photon fields other than the CMB: an optical ( $T = 4000$  K) photon field with an energy density  $u_{\text{opt}} = 0.5 \text{ eV cm}^{-3}$ , and an IR ( $T = 40$  K) photon field with an energy density  $u_{\text{ir}} = 0.5 \text{ eV cm}^{-3}$  or  $u_{\text{ir}} = 2.0 \text{ eV cm}^{-3}$  – finding that  $\eta_B$ ,  $E_{\text{break}}$ , and the parameters associated with the energetics of the neutron star ( $\tau_{\text{sd}}$ ,  $t_{\text{age}}$ ,  $\dot{E}_0$ , and  $P_0$ ) depend on  $u_{\text{ir}}$  (Tanaka & Takahara 2011). As listed in Table 3, in general our parameters agree – though their analysis favors a higher value of  $P_0$  (less energetic neutron star) due to the inclusion of these additional photon fields.

Similar results were obtained by Torres et al. (2014), which uses an evolutionary model that includes the diffusion of particles both inside and out of the PWN (Martin et al. 2012). Like Tanaka & Takahara (2011), they include emission from electrons inverse Compton scattering off two photon fields in addition to the CMB, one with  $T_{\text{FIR}} = 20$  K and energy density  $u_{\text{FIR}} = 2.0 \text{ eV cm}^{-3}$  and the other with  $T_{\text{NIR}} = 3000$  K and energy density  $u_{\text{FIR}} = 1.1 \text{ eV cm}^{-3}$  (Torres et al. 2014) – again deriving a lower  $\dot{E}_0$  (higher  $P_0$ ) than our analysis. This model also assumes the maximum energy of particles is limited by confinement in the termination shock – finding that the current value of  $E_{\text{max}}$  is similar to what we require for our model.

Lastly, we compare our results with those of Li et al. (2010), who model the broadband SED of G54.1+0.3 for both a leptonic and combined leptonic and hadronic origin for the observed  $\gamma$ -rays. Like Torres et al. (2014), they allowed the maximum energy of particles injected at the termination shock  $E_{\text{max}}$  to vary, setting it to the energy whose Larmor radius is the radius of the PWN (Li et al. 2010). Their model also allows leptons to escape from the PWN, and that these particles inverse Compton scatter off the CMB, background IR and optical photons from the Milky Way, and emission from the IR “loop” and its embedded point sources around this PWN (Koo et al. 2008; Temim et al. 2010). In the

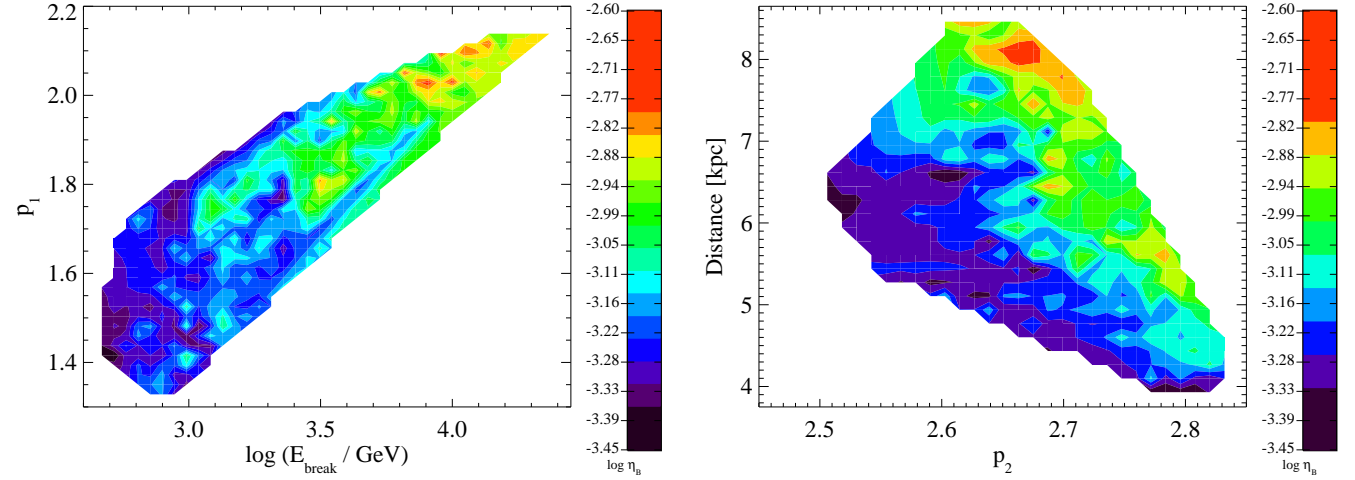


**Figure 7.** The magnetization of the pulsar wind  $\eta_B$  (color scale) for different values of the break energy  $E_{\text{break}}$  and low-energy particle index  $p_1$  (*right*) and distance  $d$  and high energy particle index  $p_2$  (*left*). Both are calculated for trials with  $\chi^2 < 7.10$  (the  $3\sigma$  parameter space).

**Table 3**

The 90% Confidence Interval of the Properties of G54.1+0.3 Derived from our Analysis, Compared with Values Derived from Previous Analyses of this Source.

PARAMETER	This Work	Chevalier (2005)	Bocchino et al. (2010)	Li et al. (2010)	Tanaka & Takahara (2011)	Torres et al. (2014)
$E_{\text{sn}}$ ( $10^{51}$ ergs)	0.08 – 1.5	$\equiv 1$	0.3 – 1.6	...	...	$\equiv 1$
$M_{\text{ej}}$ ( $M_{\odot}$ )	5.7 – 44	$\equiv 5$	$\equiv 8$	...	...	$\equiv 20$
$n_{\text{ism}}$ ( $\text{cm}^{-3}$ )	$(0.03 - 6.3) \times 10^{-3}$	...	$\sim 0.2$	...	...	$\equiv 10$
Distance (kpc)	4.6 – 8.1	$\sim 5$	$\equiv 6.2$	$\equiv 6.2$	$\equiv 6.2$	$\equiv 6$
Braking Index $p$	1.90 – 2.93	$\equiv 3$	$\equiv 3$	$\equiv 3$	$\equiv 3$	$\equiv 3$
$\tau_{\text{sd}}$ (years)	280 – 3500	$\approx 1400$	$\equiv 3$	...	600 / 1200	1171
$\eta_B$	$(0.44 - 2.2) \times 10^{-3}$	$\equiv \frac{3}{7}$	...	$\sim 1.5 \times 10^{-3}$	$0.3 \times 10^{-3} / 2 \times 10^{-3}$	$5 \times 10^{-3}$
$E_{\text{min}}$ (GeV)	0.31 – 15	...	...	$\equiv 0.05$	$< 10$	...
$E_{\text{break}}$ (TeV)	0.71 – 11	...	...	$\equiv 0.26$	0.15 / 0.09	0.3
$E_{\text{max}}$ (PeV)	0.96 – 2700	...	...	Variable	$> 0.5$	0.38 (Variable)
$p_1$	1.43 – 2.08	$\equiv 1.26$	...	$\equiv 1.2$	1.2	1.2
$p_2$	2.60 – 2.78	$\equiv 2.8$	...	$\sim 2.8$	2.55	2.8
Age [years]	2100 – 3600	$\approx 1500$	1800 – 3300	$\sim 2900$	2300 / 1700	1700
$\dot{E}_0$ [ $\text{ergs s}^{-1}$ ]	$(0.06 - 2.5) \times 10^{39}$	$\approx 5.1 \times 10^{37}$	$\equiv 4 \times 10^{38}$	$\equiv 1.4 \times 10^{39}$	$2.9 \times 10^{38} / 6.9 \times 10^{37}$	$7.2 \times 10^{37}$
$P_0$ [ms]	32 – 84	$\approx 100$	$\equiv 56$	...	62 / 87	87

*Note:* Chevalier (2005) do not specify a braking index  $p$  for this neutron star, and the quoted values of  $\tau_{\text{sd}}$  and  $\dot{E}_0$  are calculated assuming  $p \equiv 3$  for the age derived in their analysis. As described in Section 3.2.1, Tanaka & Takahara (2011) calculate the properties of this PWN assuming two different energy densities of the background IR photon field, with the values to the left of the “/” inferred for a lower energy density while the values to the right are those inferred for a higher energy density.

the pulsar wind (Section 4.3).

#### 4.1. Progenitor Star

The initial kinetic energy  $E_{\text{sn}}$  and mass  $M_{\text{ej}}$  ejected in a core-collapse supernova depends on the initial mass, metallicity, and evolution of the progenitor star (e.g., Heger et al. 2003). G54.1+0.3 has a galactocentric radius ( $\sim 6.5 - 7.5$  kpc for the favored distance of  $d \sim 5 - 8$  kpc) similar to the Sun’s ( $\sim 8 - 8.5$  kpc; Andrievsky et al. 2002a,b), suggesting its progenitor had approximately Solar metallicity. A massive star in a bi-

2. have extremely high ( $\sim 50 M_{\odot}$ ) initial mass but explodes after shedding much of this mass as a Wolf-Rayet star, resulting in a low ( $\lesssim 3 M_{\odot}$ ) ejecta mass.

As shown in Figure 2, a “canonical” supernova explosion energy of  $E_{\text{sn}} \sim (0.3 - 1) \times 10^{51}$  ergs requires a higher ejecta mass ( $M_{\text{ej}} \gtrsim 10 M_{\odot}$ ; Figure 2).

We can further constrain these parameters using the properties inferred from an analysis of the IR spectrum of the material surrounding the PWN (Koo et al. 2008; Tanaka et al. 2010). This analysis indicates that the



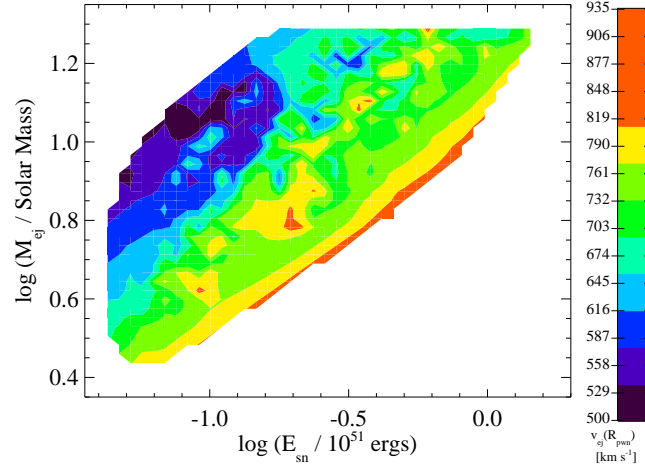


**Figure 8.** The expected expansion speed of the ejecta just outside the PWN  $v_{ej}(R_{pwn})$  for different values of the initial kinetic energy  $E_{sn}$  and mass  $M_{ej}$  of the supernova ejecta for trials with  $\chi^2 < 7.10$ ,  $M_{ej} < 20 M_{\odot}$ , and  $p < 3$ .

2003). This progenitor mass is further supported by the identification of O and B stars embedded inside the SN ejecta dust surrounding this PWN (Temim et al. 2010). Therefore, G54.1+0.3 was likely produced by the core-collapse of a  $\sim 15 - 20 M_{\odot}$  star in a massive star cluster – possibly the most massive member of this cluster, and therefore the first to explode.

This progenitor mass, and association with an massive star cluster, can explain the low ISM density  $n_{ism}$  required by our model (Table 3). The winds of main-sequence massive stars are thought to create low-density bubble with a radius  $R_b$  (Chen et al. 2013):

$$R_b = \left[ (1.22 \pm 0.04) \frac{M}{M_{\odot}} - (9.16 \pm 1.77) \right] \left( \frac{P_{ism}/k_B}{10^5 \text{ cm}^{-3} \text{ K}} \right)^{-\frac{1}{3}} \quad (12)$$

$$\sim 7 - 18 \left( \frac{P_{ism}/k_B}{10^5 \text{ cm}^{-3} \text{ K}} \right)^{-\frac{1}{3}} \text{ pc},$$

where  $P_{ism}$  is the pressure of the medium outside the wind bubble and  $k_B$  is Boltzmann’s constant. For a distance of  $\sim 4.5 - 9$  kpc (Leahy et al. 2008), this bubble will have an angular size of  $\theta_b \sim 2.7 - 14'$ . Winds from the additional massive stars in the cluster will only increase the size of this bubble, increasing the likelihood that the SNR is expanding inside a low density environment.

#### 4.2. Neutron Star Formation and Evolution

The birth properties of a neutron star reflect the physics of its formation. The initial spin period  $P_0$  and surface magnetic field of the neutron star depend

the neutron star is limited by gravitational waves resulting from r-mode instabilities generated by the “fall-back” of material during the supernova onto the proto-neutron star, the  $B_{ns} = 1.0 \times 10^{13}$  G dipole surface magnetic field strength inferred from the timing properties of PSR J1930+1852 (Camilo et al. 2002) requires  $P_0 \sim 30 - 80$  ms (Watts & Andersson 2002) – consistent with the range favored by our model (Table 3).

#### 4.3. Pulsar Wind

The rotation of the neutron star generates a strong electric potential (voltage)  $\Phi$  at its magnetic poles responsible for both creating particles in its magnetosphere (e.g., Goldreich & Julian 1969). The pulsar wind consists of particles which exit the magnetosphere along open field lines, expected to occur at a minimum rate  $\dot{N}_{GJ}$

$$\dot{N}_{GJ} = \frac{c\Phi}{e} = 7.6 \times 10^{33} \left( \frac{I_{45}}{P_{33}^3} \frac{\dot{P}}{4 \times 10^{-13} \text{ s/s}} \right)^{\frac{1}{2}} \text{ s}^{-1} \quad (13)$$

(Goldreich & Julian 1969; Bucciantini et al. 2011) where the neutron star’s moment of inertia is  $I = I_{45} \times 10^{45} \text{ g cm}^2$ ,  $P_{33} = P/33$  ms, and  $\dot{P}$  is the neutron star’s period-derivative. However, how particles are both created and leave the neutron star magnetosphere is poorly understood.

If particles are neither created nor destroyed between the light cylinder and the termination shock, we can calculate the rate particles leave the magnetosphere  $\dot{N}$  for a particular trial using Equations 2 and 3. Our assumption that the parameters regulating the spectrum of particles injected at the termination shock ( $E_{min}$ ,  $E_{break}$ ,  $E_{max}$ ,  $p_1$ , and  $p_2$ ; Table 1) are constant results in  $\dot{N} \propto \dot{E}$  over the life time of the PWN. As result, in our model the multiplicity of the pulsar wind  $\kappa$

$$\kappa \equiv \frac{\dot{N}}{\dot{N}_{GJ}}, \quad (14)$$

varies with time. Therefore, in addition to calculating the current multiplicity  $\kappa_{now}$ , we also calculate the time-integrated multiplicity  $\kappa_{int}$  (e.g., de Jager 2007):

$$\kappa_{int} = \frac{\int_0^{t_{age}} \dot{N} dt}{\int_0^{t_{age}} \dot{N}_{GJ} dt}. \quad (15)$$

Our analysis of G54.1+0.3 indicates that  $\kappa_{now} \approx 10^3$   $\kappa_{int} \sim (1 - 3) \times 10^5$  – both in good agreement with the values derived from similar analyses of other PWNe



Near the neutron star, the pulsar wind is expected to be highly magnetized ( $\eta_B \approx 1$ ). However, our model requires that  $\eta_B \sim 10^{-3}$  (Table 3) when the pulsar wind is injected into the PWN – requiring that magnetic energy is converted to particle energy between the neutron star’s light cylinder and the termination shock (e.g., Kirk & Skjæraasen 2003). Currently, magnetic reconnection in this region is thought to transform the pulsar wind from a strongly magnetized to a weakly magnetized outflow (e.g., Kirk & Skjæraasen 2003; Sironi & Spitkovsky 2011, 2014). Efficient magnetic reconnection requires that (Kirk & Skjæraasen 2003):

$$\mu < 3 \left( \frac{\pi^3 e^2}{m_e^2 c^5} \dot{E} \right)^{\frac{1}{4}} \quad (16)$$

where  $e$  and  $m_e$  are, respectively, the charge and mass of a positron,  $c$  is the speed of light, and  $\mu$ , the energy per unit mass energy of the pulsar wind, is (Kirk & Skjæraasen 2003):

$$\mu \equiv \frac{\dot{E}}{\dot{N} m c^2}, \quad (17)$$

equivalent to the bulk Lorentz factor of the pulsar wind  $\gamma_w$  before it reaches the termination shock (i.e., “upstream” from the shock). Therefore, magnetic reconnection is viable as long as the spin-down luminosity of PSR J1930+1852 is:

$$\dot{E} > \frac{m_e^2 c^5 \mu^4}{81 \pi^3 e^2} \approx (0.2 - 1.3) \times 10^{35} \frac{\text{ergs}}{\text{s}}, \quad (18)$$

for  $\mu \approx (1.5 - 2.5) \times 10^5$  as favored by our model. Since this critical  $\dot{E}$  is well below its current  $\dot{E} \approx 1.7 \times 10^{37} \frac{\text{ergs}}{\text{s}}$  (Camilo et al. 2002), magnetic reconnection should occur in the pulsar wind before it reaches the termination shock – possibly explaining the weakly magnetized pulsar wind required by our model.

Recent numerical simulations suggest that magnetic reconnection in the pulsar wind will produce particles whose spectrum is well described by a power-law with particle index  $p \lesssim 2$ , as required by our model for  $E < E_{\text{break}}$  (Table 3), up to an energy :

$$E_{\text{max, recon}} \sim m_e c^2 \left[ \frac{(\sigma_{\text{recon}} + 1)(2 - p)}{(p - 1)} \right]^{\frac{1}{2-p}}, \quad (19)$$

if the ratio of magnetic to particle energy in the magnetic reconnection region is  $\sigma_{\text{recon}} \gtrsim 10$  (Sironi & Spitkovsky 2014). We can test if this is plausible calculating  $\sigma_{\text{recon}}$  if, in Equation 19,  $p = p_1$  and  $E_{\text{max, recon}} = E_{\text{break}}$ :

Bucciantini et al. 2011), where  $\Phi$  is the voltage of the pulsar’s magnetosphere:

$$\Phi = \sqrt{\frac{\dot{E}}{c}}. \quad (21)$$

The current spin-down luminosity  $\dot{E}$  of PSR J1930+1852 (Camilo et al. 2002) would suggest that  $E_{\text{max}} \approx 6$  PeV in its magnetosphere – consistent with the values  $E_{\text{max}}$  required by our modeling (Table 3). Another possibility is that these particles are created by additional acceleration at the termination shock. Simulations suggest that efficient acceleration of an electron-positron plasma in this region requires  $\eta_B \lesssim 10^{-3}$  (e.g., Sironi et al. 2013), again consistent with the range of values favored by our modeling. The maximum particle energy is expected to be limited by either synchrotron cooling or diffusion away from the termination shock, with the theoretic maximum energy  $E_{\text{max, theory}}$  being the lower of the two. For the pulsar wind properties favored by our modeling, the maximum energy of the particles accelerated at the termination shock is limited by diffusion, such that: (Sironi et al. 2013):

$$E_{\text{max, theory}} \simeq 1.9 \times 10^7 m_e c^2 \left( \frac{\dot{E}}{10^{38.5} \frac{\text{ergs}}{\text{s}}} \right)^{\frac{3}{4}} \left( \frac{\dot{N}}{10^{40} \text{ s}^{-1}} \right)^{-\frac{1}{2}} \quad (22)$$

~ 15 – 25 PeV. (23)

Since  $\sim 50\%$  of our trials have  $E_{\text{max}} < E_{\text{max, theory}}$ , our results are also consistent with highest energy particles being produced at the termination shock.

Lastly, numerical simulations suggest the spectral shape of particles injected into the PWN at the termination shock depends strongly on the structure of the unshocked pulsar wind (e.g., Sironi & Spitkovsky 2011). When it leaves the neutron star magnetosphere, the pulsar wind is expected to be primarily equatorial and composed of regions of alternating magnetic field directions (e.g., Bogovalov 1999) of width  $\lambda$ . The shape of the resultant particle spectrum is expected to depend on (Sironi & Spitkovsky 2011):

$$\frac{\lambda}{r_L \sigma} \simeq 4 \pi \kappa \frac{R_{\text{LC}}}{R_{\text{TS}}}, \quad (24)$$

where  $r_L$  and  $\sigma$  are, respectively, the relativistic Larmor radius and magnetization of the unshocked pulsar wind,  $\kappa$  is the multiplicity (Equation 14),  $R_{\text{TS}}$  is the radius of the termination shock,  $R_{\text{LC}}$  is the radius of the light cylinder:

$$R_{\text{LC}} = \frac{cP}{2\pi} \quad (25)$$

$\dot{N}_{\text{GJ}} \approx 4.69 \times 10^{34} \text{ s}^{-1}$  and  $R_{\text{LC}} \approx 6.53 \times 10^8 \text{ cm}$ . Additionally, analysis of a *Chandra* observation identified a ring with semi-major axis  $\theta_{\text{TS}} = 5''.7$  centered on the pulsar, which is believed to mark the position of the termination shock in this PWN (Lu et al. 2002; Temim et al. 2010). For these values, the trial parameters with the lowest  $\chi^2$  favor  $\frac{\lambda}{r_{\text{L}}\sigma} \sim 10^{-5} - 10^{-4}$ , in contradiction with the results of Sironi & Spitkovsky (2011).

## 5. OBSERVATIONAL TESTS

While our evolutionary model for a PWN inside an SNR (Section 2) reproduces the observed properties of G54.1+0.3 for a wide range in parameter space (Table 3), it is important to test the validity of this model by predicting the value of additional observable properties. Thanks to our parameter exploration, not only can we predict the values of future observations, we can also estimate the resulting improvement in the allowed physical parameters. For these predictions, we only use trials with  $\chi^2 < 7.10$ ,  $M_{\text{ej}} < 20 M_{\odot}$ , and  $p < 3.0$ . We only consider trials with  $M_{\text{ej}} < 20 M_{\odot}$  since stellar evolution models suggests this is the maximum ejecta mass possible for a Solar metallicity star (Woosley et al. 2002; Heger et al. 2003; Heger 2015, private communication), and only trials with  $p < 3$  since  $p > 3$  has yet to be measured from any isolated neutron star (e.g., Livingstone 2011).

Our model can predict properties of the SNR around G54.1+0.3 not yet measured, for example its expansion velocity  $v_{\text{snr}}$ . Due to the young age and low ISM density preferred by our model, we predict an extremely fast  $v_{\text{snr}} \sim 3000 \text{ km s}^{-1}$  – among the highest measured or inferred for any other SNR (e.g., Ghavamian et al. 2007). This suggests the identified radio and X-ray shell may not actually be a SNR but the progenitor’s stellar wind bubble (Section 4.1). This can be determined by the measuring its radio spectral index ( $\alpha$ , where flux density  $S_{\nu} \propto \nu^{\alpha}$ ), since the free-free emission expected to dominate the radio emission from a stellar wind bubble has  $\alpha \gtrsim 0$  while SNRs typically have  $\alpha \sim -0.7$ . If future studies indicate this is a stellar wind bubble, our model would still favor a  $\sim 15 - 20 M_{\odot}$  progenitor based on the properties of the IR emission around the PWN (Section 4.1), but would offer much weaker constraints on the density of the surrounding ISM.

We can also predict currently unmeasured properties of the PWN, and determine what can be gained from their measurement. For example, our model predicts the average angular radius of the PWN is expanding by  $\dot{\theta}_{\text{pwn}} \sim 20 - 50 \text{ mas year}^{-1}$ , and this value is sensitive to the mass  $M_{\text{ej}}$  and initial kinetic energy  $E_{\text{sn}}$  of the supernova ejecta because the PWN has not yet collided with the SNR reverse shock (Figure 9). This is po-

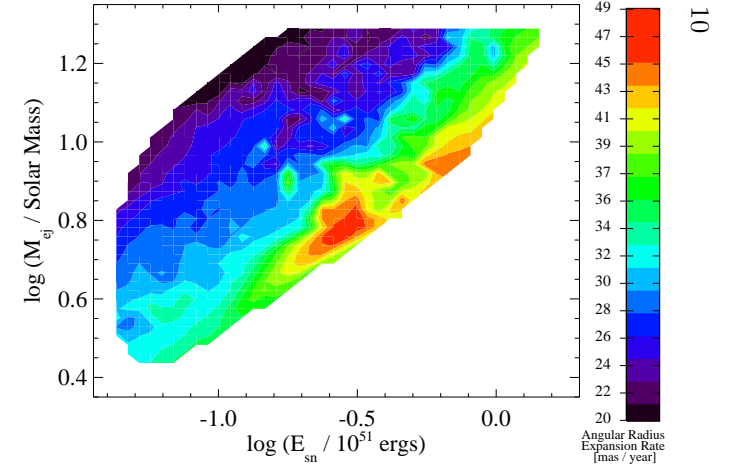


**Figure 9.** The expected angular expansion rate of this PWN’s radius  $\dot{\theta}_{\text{pwn}}$  for different values of the initial kinetic energy  $E_{\text{sn}}$  and mass  $M_{\text{ej}}$  of the supernova ejecta for trials with  $\chi^2 < 7.10$ ,  $M_{\text{ej}} < 20 M_{\odot}$ , and  $p < 3$ .

tion shock  $E_{\text{min}}$  (Figure 11). All four of these quantities are measurable by new observing facilities such as LOFAR (van Haarlem et al. 2013). Lastly, we find that the absorbed 5 – 80 keV flux of G54.1+0.3, measurable by the *NuSTAR* satellite (Harrison et al. 2013), is strongly depends with the distance to this source (Figure 12) – likely a result of the parameter degeneracies discussed in Section 3.2.

## 6. SUMMARY AND CONCLUSIONS

In summary, we have fit the observed properties of G54.1+0.3 using a one-zone model for the evolution of a PWN inside an SNR (Section 2). This model can reproduce its observed properties (Section 3.1), and suggests that the progenitor was an isolated  $\sim 15 M_{\odot}$  star, most likely the member of a massive star cluster, which exploded in a low density environment possibly produced by its stellar wind (Section 4.1). The resultant neutron star, PSR J1930+1852, had an initial spin period  $P_0 \sim 30 - 80 \text{ ms}$  (Section 4.2). Our model requires that the current multiplicity of particle production in its magnetosphere is  $\kappa \sim (1 - 3) \times 10^5$ , and suggests that the magnetosphere electric potential is sufficient to accelerate particles to the highest energies  $E_{\text{max}}$  required by our model. The low magnetization of the pulsar wind and low-energy component of particle spectrum can be attributed to acceleration resulting from magnetic reconnection between the light cylinder and the termination shock, though our model suggests the “stripes” in the unshocked pulsar wind are too narrow for acceleration at the termination shock to produce the broken power-

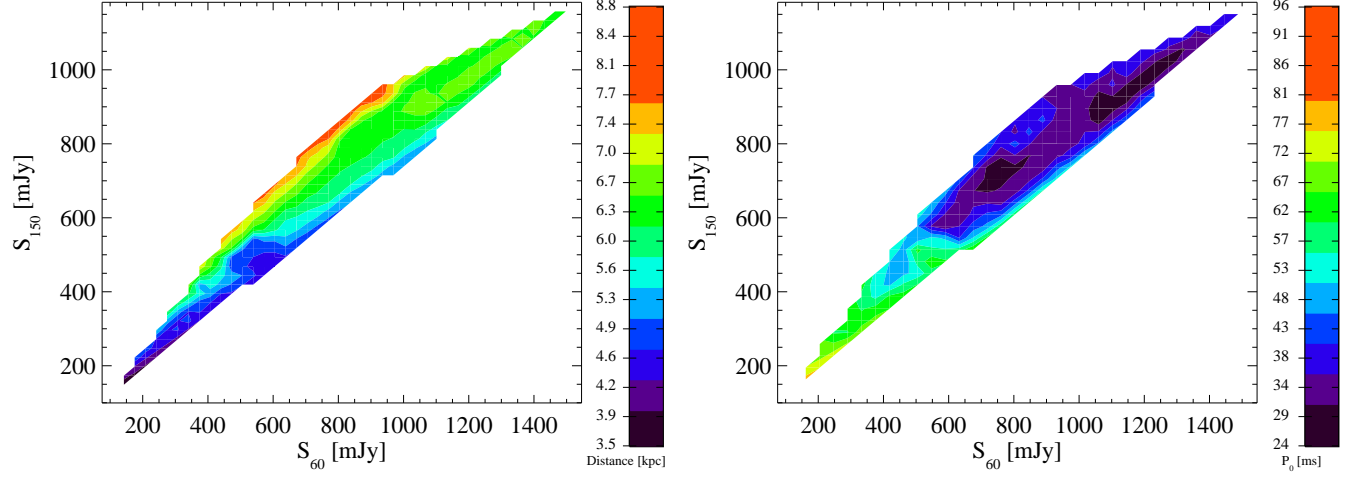


**Figure 10.** The distance  $d$  to G54.1+0.3 (*left*) and initial spin period  $P_0$  of PSR J1930+1852 (*right*) for the values of the 60 MHz  $S_{60}$  and 150 MHz  $S_{150}$  flux densities predicted by trials with  $\chi^2 < 7.10$ ,  $M_{\text{ej}} < 20 M_{\odot}$ , and  $p < 3$ .

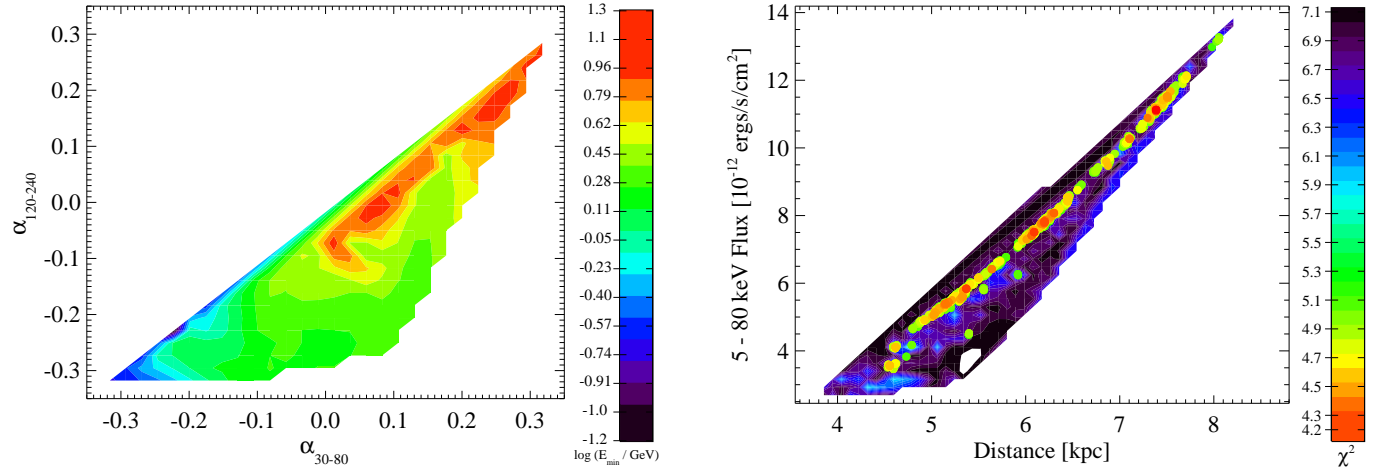


**Figure 11.** The minimum energy in the pulsar wind  $E_{\text{min}}$  for the 30–80 MHz ( $\alpha_{30-80}$ ) and 120–240 MHz ( $\alpha_{120-240}$ ) spectral indices of G54.1+0.3 predicted by trials with  $\chi^2 < 7.10$ ,  $M_{\text{ej}} < 20 M_{\odot}$ , and  $p < 3$ .

Aliu for information regarding the GeV spectrum, and Roger Chevalier, Vikram Dwarkadas, Daniel Patnaude, and Lorenzo Sironi for useful advice.

#### REFERENCES

- Acciari, V. A., Aliu, E., Arlen, T. et al., & Zitzer, B. 2010, *ApJ*, 719, L69  
 Andrievsky, S. M., Bersier, D., Kovtyukh, V. V., et al. 2002a, *A&A*, 384, 140  
 Andrievsky, S. M., Kovtyukh, V. V., Luck, R. E., et al. 2002b,

**Figure 12.** The  $\chi^2$  for trials with different distances  $d$  and predicted 5–80 keV flux, which red signifying a lower  $\chi^2$  (better fit) and black a higher  $\chi^2$  (worse fit). Only the results of trials with  $\chi^2 < 7.10$ ,  $M_{\text{ej}} < 20 M_{\odot}$ , and  $p < 3$  are shown, and the dots indicate trials with  $\chi^2 < 5.10$  and are included to better demonstrate the degeneracy between these two parameters. The clumpiness of these points primarily reflects the sampling of the parameter space by our MCMC algorithm.

- Chevalier, R. A. 2005, *ApJ*, 619, 839  
 de Jager, O. C. 2007, *ApJ*, 658, 1177  
 Endeve, E., Cardall, C. Y., Budiardja, R. D., et al. 2010, *ApJ*, 713, 1219  
 Fang, J. & Zhang, L. 2010, *A&A*, 515, A20+  
 Gaensler, B. M. & Slane, P. O. 2006, *ARA&A*, 44, 17  
 Gelfand, J. D., Gaensler, B. M., Slane, P. O., et al. 2007, *ApJ*, 663, 468

- Kennel, C. F. & Coroniti, F. V. 1984a, *ApJ*, 283, 694  
—, 1984b, *ApJ*, 283, 710  
Kirk, J. G. & Skjæraasen, O. 2003, *ApJ*, 591, 366  
Koo, B.-C., McKee, C. F., Lee, J.-J., et al. 2008, *ApJ*, 673, L147  
Lang, C. C., Wang, Q. D., Lu, F., et al. 2010, *ApJ*, 709, 1125  
Leahy, D. A., Tian, W., & Wang, Q. D. 2008, *AJ*, 136, 1477  
Li, H., Chen, Y., & Zhang, L. 2010, *MNRAS*, 408, L80  
Livingstone, M. A. 2011, PhD thesis, McGill University (Canada)  
Lu, F., Wang, Q. D., Gotthelf, E. V. et al. 2007, *ApJ*, 663, 315  
Lu, F. J., Aschenbach, B., & Song, L. M. 2001, *A&A*, 370, 570  
Lu, F. J., Wang, Q. D., Aschenbach, B., et al. 2002, *ApJ*, 568, L49  
Martin, J., Torres, D. F., & Rea, N. 2012, *ArXiv e-prints*  
Olmi, B., Del Zanna, L., Amato, E., et al. 2014, *MNRAS*, 438, 1518  
Ott, C. D., Burrows, A., Thompson, T. A., et al. 2006, *ApJS*, 164, 130  
Porth, O., Komissarov, S. S., & Keppens, R. 2013, *MNRAS*, 431, L48  
—, 2014, *MNRAS*, 438, 278  
Reynolds, S. P. & Chevalier, R. A. 1984, *ApJ*, 278, 630  
Sironi, L. & Spitkovsky, A. 2011, *ApJ*, 741, 39  
—, 2014, *ApJ*, 783, L21  
Sironi, L., Spitkovsky, A., & Arons, J. 2013, *ApJ*, 771, 54  
Spitkovsky, A. 2008, *ApJ*, 682, L5  
Tanaka, S. J. & Takahara, F. 2010, *ApJ*, 715, 1248  
—, 2011, *ApJ*, 741, 40  
Temim, T., Slane, P., Reynolds, S. P., et al. 2010, *ApJ*, 710, 309  
Torres, D. F., Cillis, A., Martín, J., & de Oña Wilhelmi, E. 2014, *Journal of High Energy Astrophysics*, 1, 31  
van Haarlem, M. P., Wise, M. W., Gunst, A. W., et al. 2013, *A&A*, 556, A2  
Volpi, D., Del Zanna, L., Amato, E., et al. 2008, *A&A*, 485, 337  
Watts, A. L. & Andersson, N. 2002, *MNRAS*, 333, 943  
Woosley, S. E., Heger, A., & Weaver, T. A. 2002, *Rev. Mod. Phys.*, 74, 1015  
Zwicky, F. 1938, *ApJ*, 88, 522